



Single Acetylation-mimetic Mutation in TDP-43 Nuclear Localization Signal Disrupts Importin α 1/ β Signaling

Ying-Hui Ko¹, Ravi K. Lokareddy¹, Steven G. Doll^{2,3}, Daniel P. Yeggoni⁴, Amandeep Girdhar², Ian Mawn², Joseph R. Klim⁵, Noreen F. Rizvi⁵, Rachel Meyers⁵, Richard E. Gillilan⁶, Lin Guo^{2,*} and Gino Cingolani^{1,*}

1 - Dept. of Biochemistry and Molecular Genetics, The University of Alabama at Birmingham, 1825 University Blvd, Birmingham, AL 35294, USA

2 - Dept. of Biochemistry and Molecular Biology, Thomas Jefferson University, 1020 Locust Street, Philadelphia, PA 19107, USA

3 - Dept. of Neurology, Johns Hopkins University School of Medicine, 1800 Orleans St Baltimore, Baltimore, MD 21287, USA

4 - Dept. of Cell Biology, UConn Health Center, 263 Farmington Avenue, Farmington, CT 06030, USA

5 - Faze Medicines, Cambridge, MA 02139, USA

6 - Macromolecular Diffraction Facility, Cornell High Energy Synchrotron Source (MacCHESS), Cornell University, 161 Synchrotron Drive, Ithaca, NY 14853, USA

Correspondence to Lin Guo and Gino Cingolani: lin.guo@jefferson.edu (L. Guo), gcingola@uab.edu (G. Cingolani)

<https://doi.org/10.1016/j.jmb.2024.168751>

Edited by Richard W. Kriwacki

Abstract

Cytoplasmic aggregation of the TAR-DNA binding protein of 43 kDa (TDP-43) is the hallmark of sporadic amyotrophic lateral sclerosis (ALS). Most ALS patients with TDP-43 aggregates in neurons and glia do not have mutations in the TDP-43 gene but contain aberrantly post-translationally modified TDP-43. Here, we found that a single acetylation-mimetic mutation (K82Q) near the TDP-43 minor Nuclear Localization Signal (NLS) box, which mimics a post-translational modification identified in an ALS patient, can lead to TDP-43 mislocalization to the cytoplasm and irreversible aggregation. We demonstrate that the acetylation mimetic disrupts binding to importins, halting nuclear import and preventing importin α 1/ β anti-aggregation activity. We propose that perturbations near the NLS are an additional mechanism by which a cellular insult other than a genetically inherited mutation leads to TDP-43 aggregation and loss of function. Our findings are relevant to deciphering the molecular etiology of sporadic ALS.

© 2024 Elsevier Ltd. All rights are reserved, including those for text and data mining, AI training, and similar technologies.

Introduction

Amyotrophic lateral sclerosis (ALS) is a neurodegenerative disease that affects nerve cells in the brain and spinal cord, causing loss of muscle control and affecting the vital connection needed to move, eat, and breathe. The disease is fatal, as no cure is currently available. A small number of ALS cases are inherited and can be traced to disease-causing mutations (familial ALS). However, the

overwhelming majority (90–95%) of ALS cases are sporadic and occur typically in adulthood in otherwise normal individuals. The causes of sporadic ALS involve a combination of genetic and environmental factors, such as post-translational modifications (PTMs).^{1–3} Over 95% of familial and sporadic ALS and frontotemporal lobar degeneration (FTD) patients have cytoplasmic inclusion bodies in vulnerable neurons containing aggregates of the RNA/DNA binding protein TDP-43.^{4,5} Although

TDP-43 aggregation is commonly regarded as the hallmark of ALS,^{6–13} the vast majority of ALS patients with TDP-43 aggregates do not harbor mutations in the TDP-43 gene. Instead, TDP-43 in brain aggregates is aberrantly post-translationally modified, containing phosphorylation, acetylation, and ubiquitination.^{2,4,12,14} TDP-43 aggregates also contain a mix of the full-length TDP-43 (M.W. 43 kDa) and C-terminal proteolytic fragments of smaller molecular weight (TDP-35 and TDP-25).⁹

TDP-43 is a conserved multidomain RNA/DNA-binding protein of 414 amino acids¹⁰ broadly expressed in many organs.¹⁵ It contains an N-terminal domain (NTD) implicated in dimerization, followed by a bipartite Nuclear Localization Signal (NLS), two RNA binding modules (RRMs), and a C-terminal prion-like C-terminal domain (CTD) (Figure 1A). TDP-43 plays an essential housekeeping function as a modulator of RNA splicing,^{16,17} which prevents aberrant RNA splicing and protects the transcriptome, a function central to the physiology of motor neurons, whose loss or alteration is linked to neuronal death. In 2019, several labs reported that TDP-43 regulates the splicing of the Stathmin 2 messenger RNA.^{18,19} When TDP-43 is lost or its function impaired, an aberrant splicing event in the Stathmin-2 genes introduces a stop codon and a polyadenylation signal, resulting in an 8-fold reduction of Stathmin-2, a regulator of microtubule stability. Reduced Stathmin-2 is a major feature of sporadic and familial ALS and a diagnostic marker for FTD²⁰ due to TDP-43 loss. Recently, Ma et al.²¹ found that UNC13A is one of the genes with the most significant levels of alternative splicing when TDP-43 is lost due to proteinopathy. TDP-43 represses a cryptic exon-splicing event in UNC13A, and when the protein is lost, UNC13A is diminished. Functionally, UNC13A is expressed in the nervous system²² (e.g., synapses and neuromuscular junctions), where it plays an essential role in vesicle maturation during exocytosis. Thus, TDP-43 is essential for neuronal physiology, and its loss is detrimental to neurons.

Different stimuli can trigger TDP-43 aggregation in neuronal cytoplasm and the formation of amyloid-like aggregates.²³ In familial ALS, mutations within the prion-like CTD (Figure 1A) enhance the protein stickiness, leading to cytoplasmic aggregation.² Hexanucleotide repeat expansion in the C9orf72 gene (found in ~50% of familial ALS cases) leads to dipeptide repeat peptides that exacerbate TDP-43 insolubility and phase separation.^{24,25} However, most ALS cases are sporadic, and in these patients, TDP-43 aggregation occurs by a mechanism independent of mutations in TDP-43 that includes aberrant PTMs,^{2,14,26} e.g., ubiquitination and phosphorylation²⁷ in the CTD, acetylation in the RRM,²⁸ that impairs RNA binding, and some reports of PTMs in the NLS region.² The effect of PTMs on TDP-43 is not fully understood and likely varies among PTMs: establishing a

cause-effect relationship between PTMs and aggregation is challenging, as aggregated TDP-43 may become more susceptible to modification after aggregating.²

This study focuses on poorly characterized PTMs near the TDP-43 Nuclear Localization Signal (NLS) (Figure 1A). Acetylation of K82, at position P₁' relative to the NLS and ubiquitination of K79 (position P₋₁') were found in a sarkosyl-insoluble fraction of TDP-43 aggregates isolated from brains of ALS patients.²⁹ Acetylation of TDP-43 K84 (P₃' position)³⁰ mislocalizes TDP-43 to the cytoplasm in HEK293E cells. Similarly, mutations of K84 to alanine or arginine prevented the nuclear import of a fusion protein comprising the red fluorescent protein fused to TDP-43-NLS (RFP-TDP-43-NLS).³¹ A study also found that the ALS-associated A90V mutation, C-terminal of the minor NLS box, sequesters the endogenous TDP-43 into insoluble cytoplasmic aggregates.³² In the TDP-43 NLS linker between minor and major boxes, three residues, T88, S91, and S92, were previously identified as targets of casein kinase 1- δ .^{33,34} (Figure 1A). Substitution of T88E, S91E, and S92E to mimic phosphorylation reduced the affinity of the TDP-43 NLS for the classical nuclear import system *in vitro*.³⁵ Similarly, phosphorylation of S92 was also identified in a cellular model,³⁴ although mass spectrometry of TDP-43 fragments taken from affected tissue of two ALS patients' brains did not find phosphorylation within the TDP-43 NLS.²⁹ This study, however, did not detect any fragments corresponding to TDP-43 NTD, preventing the identification of N-terminal PTMs. Contrary to the idea that phosphorylation exacerbates aggregation, a recent study found that *in vitro* phosphorylated TDP-43 (lacking phosphorylations in the NLS³³) forms dynamic liquid-like condensates,³⁶ suggesting a protective role of this PTM.³⁷

In this paper, we determine that an acetylation mimetic at position P₁' mislocalizes TDP-43 in neuroblastoma cells, obliterating binding to importins and preventing importin α 1/ β chaperone-like activity. Our work establishes the interplay between TDP-43, PTMs near the NLS, and importin α 1/ β binding, providing new insights into the biology of TDP-43 mislocalization relevant to understanding sporadic ALS.

Results

Mutations near the TDP-43 NLS minor site mislocalize TDP-43 in neuroblastoma cells

We previously reported³⁵ that the TDP-43 NLS binds importin α 1 and β (importin α 1/ β) with nanomolar affinity via the minor NLS box (Figure 1A). We also found that importin α 1/ β binding to the NLS disrupts TDP-43 N-terminal domain (NTD) dimerization.^{3,35} Here, we investigated how mutations and PTM-mimetics near TDP-43 NLS

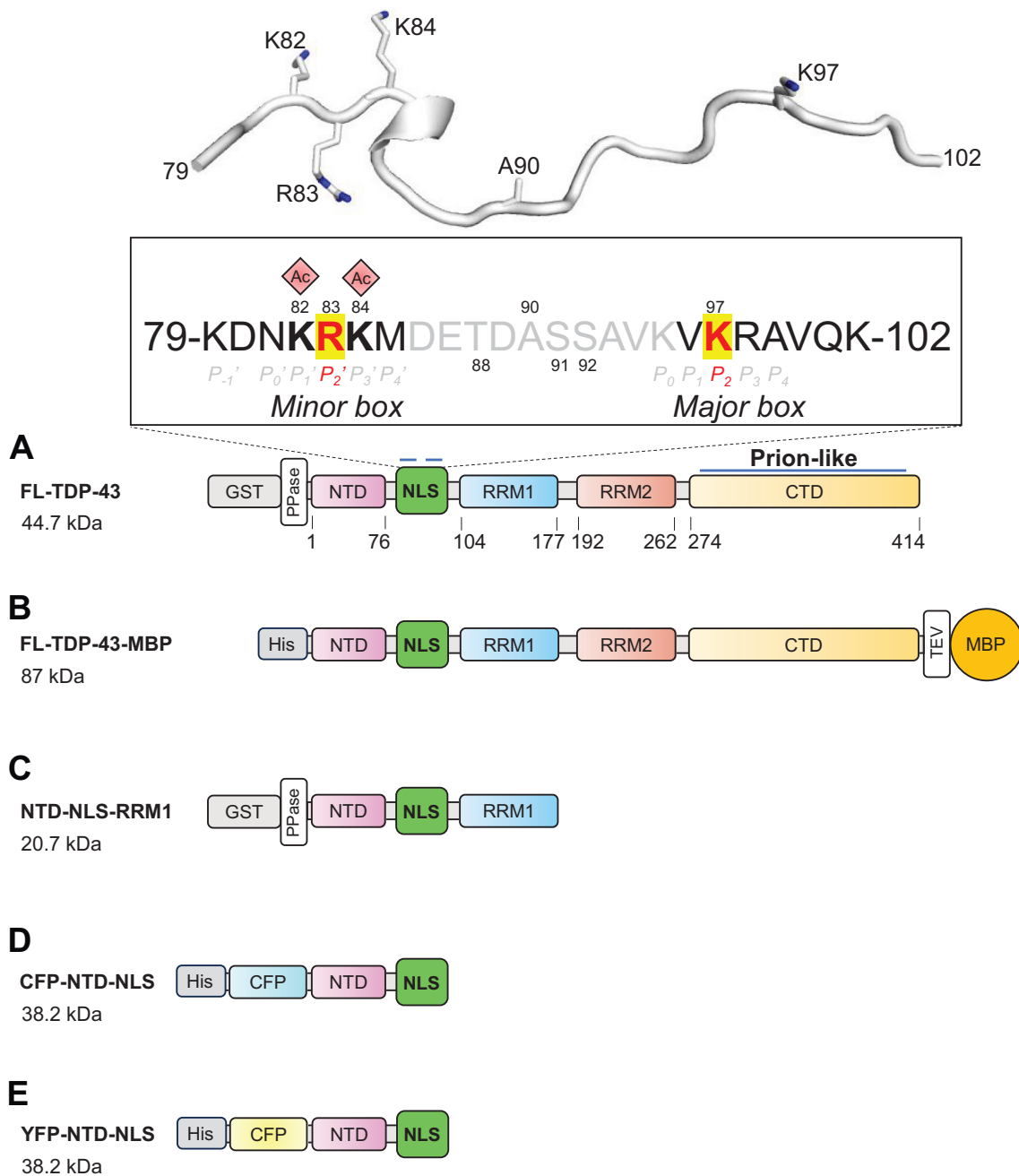


Figure 1. Schematics of all TDP-43 constructs used in this study (panels A–E). The magnified box in panel (A) shows the sequence of TDP-43 bipartite NLS. Residues contacting importin α 1 are shown in black; R83 and K97 occupying the P_2' and P_2 sites, respectively, are colored red and highlighted in yellow. Residues in the NLS that do not contact importin α 1 directly are in gray. The positions of acetylated residues studied in this paper are shown as red diamonds. A ribbon diagram of the TDP-43 NLS solved in complex with importin α (PDB id: 7N9H) is shown above the NLS amino acid sequence.

affect protein localization in a neuroblastoma cell line. We transduced SH-SY5Y cells with a collection of TDP-43 variants tagged with mCherry using lentiviral particles and sorted the cells expressing mCherry-tagged TDP-43. We then monitored TDP-43 localization using fluorescence microscopy. As previously reported,^{38,39} wt TDP-43

was primarily nuclear at steady-state with $\sim 95\%$ of the protein localized in the nucleus of SH-SY5Y cells (Figure 2A, B). We found that mutations near the minor NLS box (Figure 1A), namely the acetylation mimetic K82Q and the dominant negative mutants R83A/R83K,³⁵ dramatically affected TDP-43 localization, relocalizing the majority of TDP-43

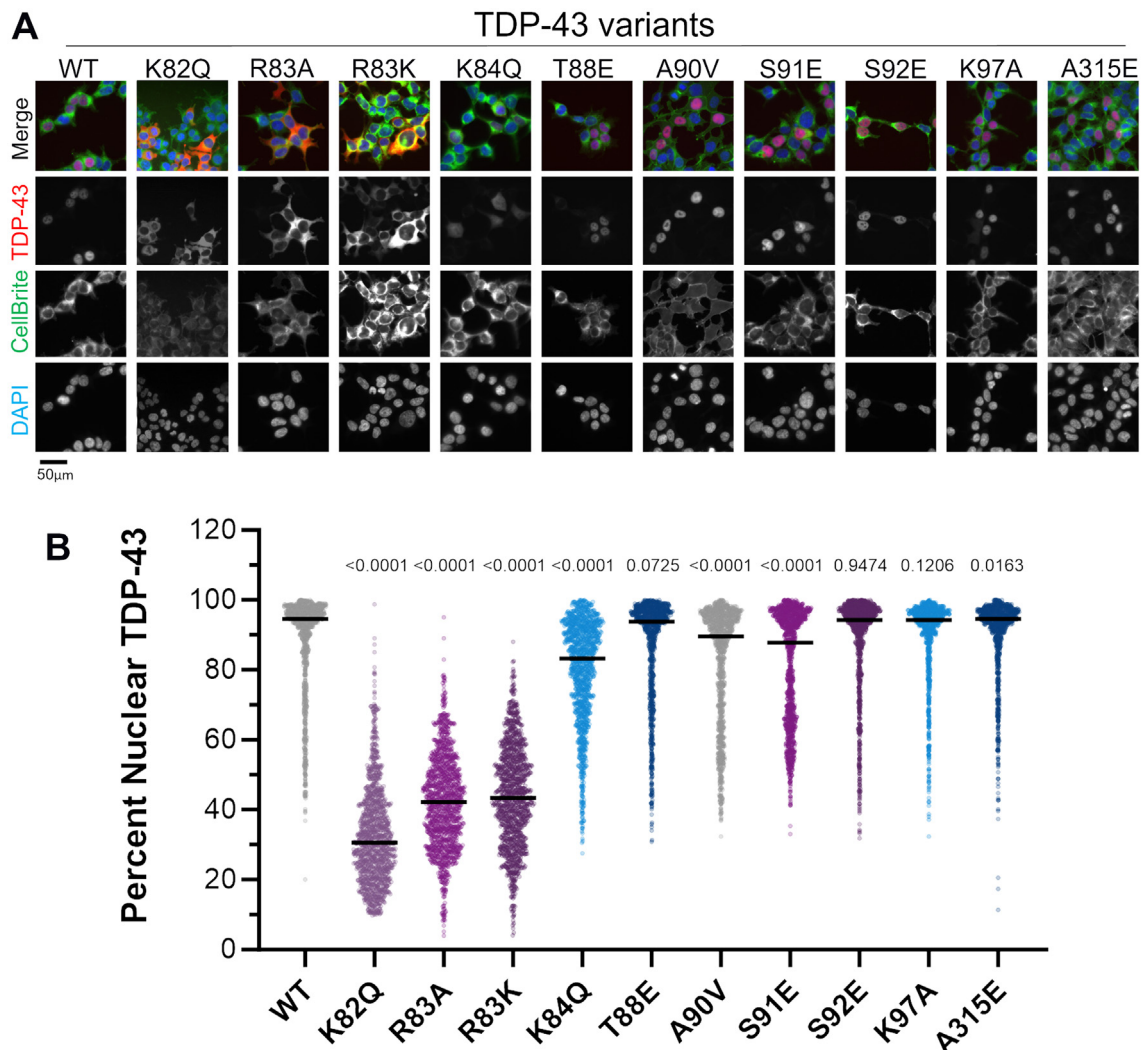


Figure 2. Subcellular localization of TDP-43 overexpressed in SH-SY5Y cells. (A) Representative micrographs of SH-SY5Y cells overexpressing indicated TDP-43 variants tagged with mCherry (red) and counterstained with DAPI (blue) and the membrane stain CellBrite (green). WT TDP-43 is in the nucleus, but K82Q, R83A, AND R83K variants are strongly localized in the cytoplasm. (B) Quantification of TDP-43 subcellular distribution from three biological replicate cell experiments ($n = 3$) quantifying ~ 1000 cells per construct. Dots represent individual cells with a median indicated by the bars. Standard Deviations are WT=14; K82Q=14.16; R83A=13.67; R83K=14.60; K84Q=15.18; T88E=14.86; A90V=16.84; S91A=16.44; S92A=13.57; K97A=11.55; A315E=11.44. Statistical analysis was performed with a one-way ANOVA using Dunnett's multiple comparisons test. Significant ($p < 0.01$) deviation from the WT TDP-43.

to the cytoplasm (Figure 2A, B), in agreement with previous reports.^{40–42} K82 occupies the P_1 position of the minor binding site residues immediately upstream of the P_2' position. This lysine engages in two hydrogen bonds with importin $\alpha 1$.³⁵ Less dramatic was the effect of the acetylation mimetic K84Q at position P_3' , which remained 70% nuclear, displaying a less strong phenotype than seen by introducing a similar mutation in a reporter protein.³¹ In contrast, TDP-43 familial mutation A90V³² and the phosphomimetic S91E³³ had a small yet statistically significant TDP-43 steady-state nuclear

localization reduction by as much as 5% (Figure 2A, B). Finally, mutations in major NLS binding site K97A, phosphomimetics T88E and S91E, and disease-associated mutations found in the CTD, A315E,² did not have statistically significant changes in TDP-43 localization that remained mainly nuclear (Figure 2A, B). Comparable results were observed using biochemical subcellular fractionation and immunoblot analysis (Figure S1A, B). Thus, mutations near the TDP-43 minor NLS box but not at the major site or CTD affect TDP-43 localization in an overexpression system.

A single acetylation mimetic at K82 disrupts binding to importin α 1/ β

To correlate TDP-43 cellular localization with binding affinity for importins, we asked how the mutations/PTM-mimetics in TDP-43 affect binding affinity for purified importin α 1/ β *in vitro*. To this end, we introduced K97A, R83A, K82Q, and K84Q in the soluble TDP-43 fragment comprising

NTD-NLS-RRM1 (Figure 1C). We then monitored the ability of these mutants to bind the importin α 1/ β complex by using an *in cellulo* pull-down assay³⁵ (Figure 3A). In this assay, importin α 1 and β were co-expressed from a polycistronic plasmid in bacteria in the presence of a second plasmid expressing GST-tagged TDP-43, either WT or point mutants. After confirming that all TDP-43 variants express to a comparable level as the WT protein

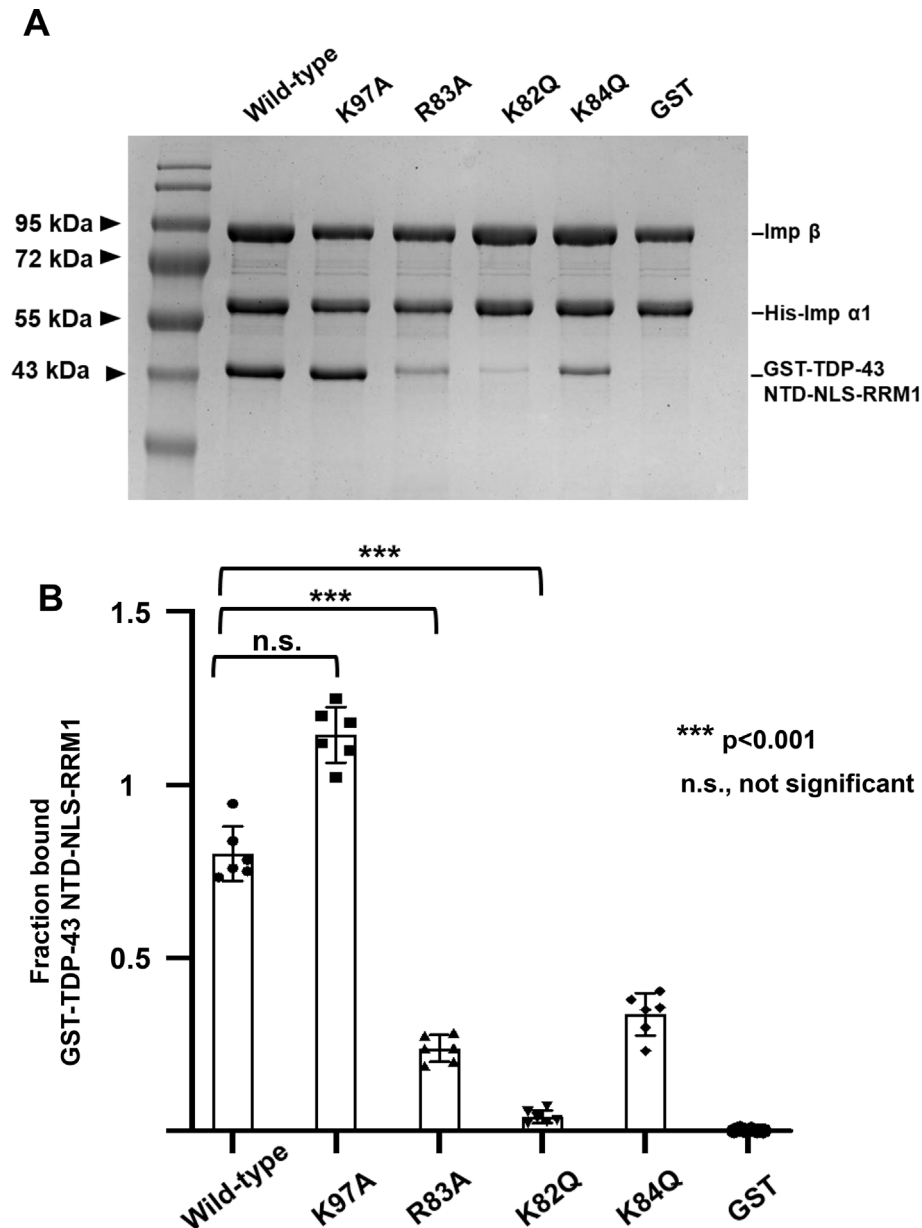


Figure 3. In cellulo pull-down assay. (A) Representative SDS-PAGE gel of the pull-down experiment in which WT TDP-43 NTD-NLS-RRM1 and mutants in TDP-43 NLS region were co-expressed with the importin α 1/ β heterodimer. (B) Quantification of GST-TDP-43-NTD-NLS-RRM1 bands from replicate SDS-PAGE gels ($n = 7$). Band intensity was measured through ImageJ.⁷² Histogram columns indicate the ratio of TDP-43 band intensity to the normalized importin α 1 intensity, with standard deviation (error bars). Significant ($p < 0.01$) deviation from the WT TDP-43: importin α 1 ratio was determined through a two-tailed Student's *t*-test assuming unequal variance. *** $p < 0.001$; n.s., not significant.

(Figure S2), equal volumes of lysate containing importin $\alpha 1$, β and TDP-43, treated under identical conditions, were immobilized on nickel agarose beads, washed and analyzed by SDS-PAGE. The results of these experiments revealed that all point mutations at the minor NLS pocket of TDP-43 affect the binding affinity to the importin $\alpha 1/\beta$ heterodimer (Figure 3A, B). The degree of disrupted binding correlates well with the degree of cytoplasmic mislocalization described in Figure 2B. As reported by Doll et al.,³⁵ the R83A mutant lacking R83 at the P₂' position showed negligible binding to importins (Figure 3A, B). Strikingly, the acetylation mimetic mutation at K82Q had the most destructive effect on importin $\alpha 1/\beta$ association to TDP-43, which is consistent with the severe cytoplasmic mislocalization of this mutant (Figure 2A, B). The second acetylation-mimetic, K84Q, reduced but did not abolish importin $\alpha 1/\beta$ binding (Figure 3A, B), in agreement with our data in neuroblastoma cells (Figure 2A, B) and previous work in a non-neuronal cell model.³⁰ An ala-mutation at K82 had a less destabilizing effect on importin $\alpha 1/\beta$ binding affinity (Figure S3A, B) than K82Q. This suggests that the presence of an acetyl group in K82 (or an amide group in the Q82 mimetic mutation) rather than the loss of a positive charge in the K82 side chain, is the primary reason for the disruption of high affinity binding to importins. Instead, K82A was indistinguishable from K82Q in our pull-down assay (Figure S3A, B). In contrast, the K97A mutation at the major NLS pocket did not affect the binding affinity for importin $\alpha 1/\beta$ (Figure 3A, B). This variant behaved like WT TDP-43 and even had slightly enhanced binding, as also found by Doll et al.³⁵ Thus, TDP-43 mislocalization in SH-SY5Y cells due to mutations at position P₁' and P₂' can be explained by loss of high-affinity binding to importin $\alpha 1/\beta$.

Importin $\alpha 1/\beta$ disrupts the TDP-43 aggregation

Importin $\alpha 1/\beta$ were shown to reduce TDP-43 aggregation *in vitro*, exerting chaperone-like activity.^{24,43} Next, we asked how mutations and PTM-mimetics in TDP-43 affect the importin $\alpha 1/\beta$ chaperone activity. We used a turbidity assay to monitor TDP-43 aggregation over time.⁴⁴ In this assay, full-length TDP-43 was fused to a C-terminal Maltose Binding Protein (MBP) affinity tag (Figure 1B) that keeps the TDP-43-M chimera soluble at 37 °C, at the concentration used in the assay (10 μ M). TDP-43 aggregation was triggered by the addition of TEV protease that cleaves MBP liberating TDP-43, which began to aggregate in a time- and temperature-dependent manner (Figure 4A, red curve). Without TEV, TDP-43-M remained soluble under identical experimental conditions (Figure 4A, blue curve), although the MBP-tagged TDP-43 was aggregation-prone on amylose beads, as shown in Figure S6). We measured turbidity at 395 nm after 50 min (denoted by an asterisk in Fig-

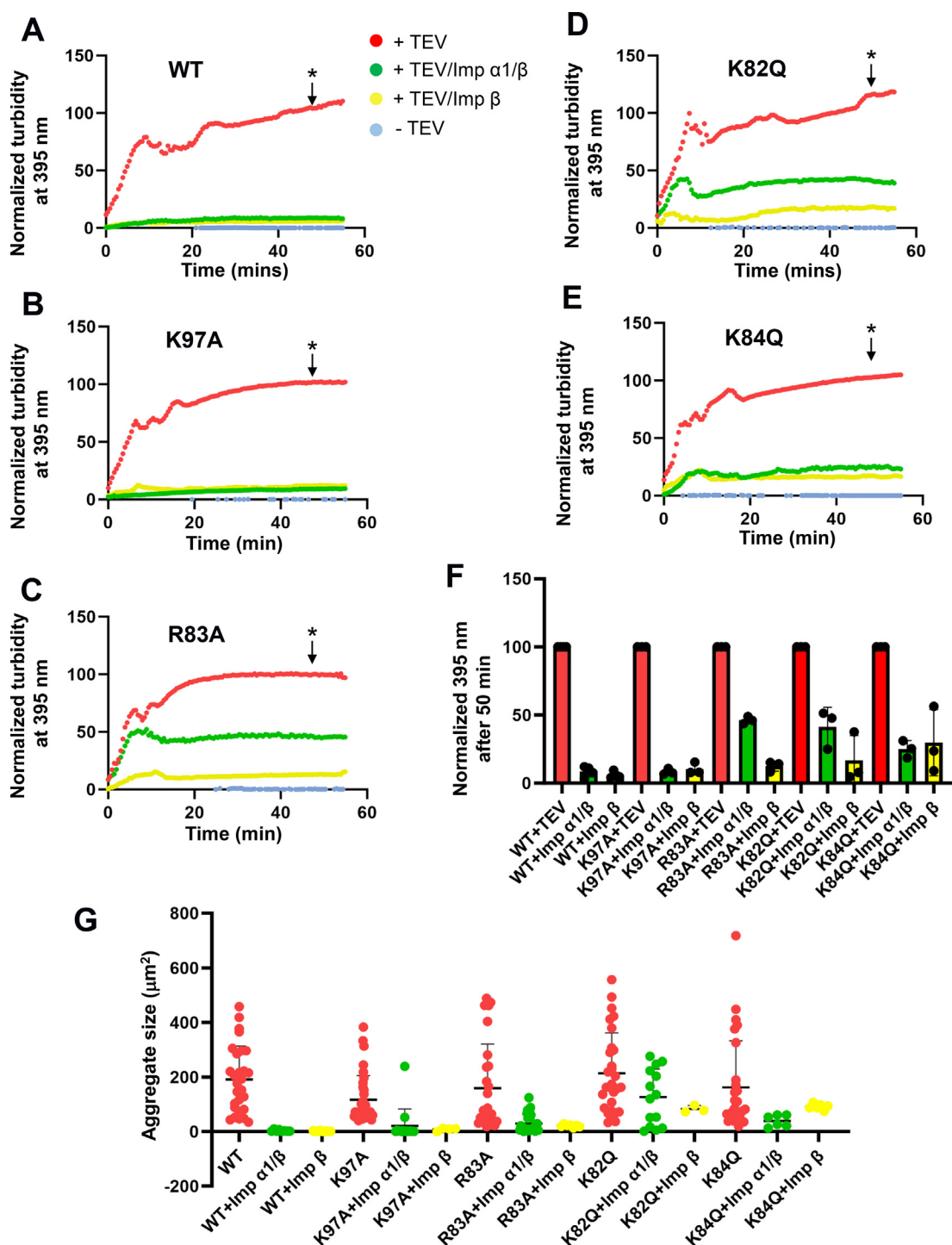
ure 4A–E) as a proxy for aggregated TDP-43 versus TDP-43 left in solution. In addition to WT TDP-43, we tested the same mutants that majorly mislocalized TDP-43 in SH-SY5Y cells (Figure 2B) and reduced binding to importin $\alpha 1/\beta$ by pull-down assay (Figure 3B), namely K97A, R83A, K82Q, and K84Q.

At first, we asked if mutations/PTM-mimetics near the NLS affect the rate of TDP-43 aggregation at 37 °C (Figure 4A–E, red curves), but found that all mutants, tested under identical experimental conditions, resulted in a comparable degree of aggregation after 50 min, quantified in Figure 4F. Next, we asked how different mutations affect the chaperone activity of importins. In the presence of a stoichiometric quantity of importin $\alpha 1/\beta$ (Figure 4A–E, green curves), or just importin β (Figure 4A–E, yellow curves), aggregation was dramatically reduced for both WT and K97A (Figure 4F). In contrast, TDP-43 variants carrying mutations K82Q and R83A were insensitive to importin $\alpha 1/\beta$ chaperone activity and had reduced sensitivity to importin β anti-aggregation activity (Figure 4F). Finally, TDP-43 carrying an acetylation mimetic at K84 was partially sensitive to either importin $\alpha 1/\beta$ or importin β chaperone activity (Figure 4E and F), displaying an intermediate behavior between K97A and K82Q.

TDP-43 aggregates' shape, size, and density in Figure 4A–E were also visualized by light microscopy after 50 min (Figure S5), at 100 \times magnification. Figure 4G shows a quantification of particle size for all TDP-43 variants. Overall, both importin $\alpha 1/\beta$ and importin β potently reduced TDP-43 aggregation *in vitro*. This effect was specific and not reproduced by an unrelated protein like the GTPase Ran (Figure S4). We also asked if importin $\alpha 1$ (or the isoform $\alpha 5$) alone were sufficient to prevent TDP-43 aggregation in a turbidity assay but found that either protein aggregated TDP-43 in the absence of importin β (*data not shown*). Thus, mutations in the TDP-43 minor NLS box affect the NLS-dependent recognition of importin $\alpha 1/\beta$ more dramatically than importin β chaperone activity.

Importin $\alpha 1/\beta$ disrupts TDP-43 dimerization via the N-terminal domain (NTD)

Doll et al. found that importin $\alpha 1/\beta$ association with TDP-43 NLS disrupts NTD dimerization. TDP-43 NTD is essentially always dimeric in solution,^{45–49} whereas the trimeric importin $\alpha 1/\beta$:TDP-43 complex is a 1:1:1 species.³⁵ We then asked if mutations/PTM mimetics in the NLS minor site interfere with importin $\alpha 1/\beta$ -mediated disruption of NTD dimerization. To this end, we generated a minimal TDP-43 construct containing only NTD and NLS (Figure 1D, E) and introduced mutations K97A, R83A, K82Q, and K84Q in the NLS region. Each NTD-NLS construct was expressed fused to an N-terminal Cyan Fluorescent Protein (CFP) or



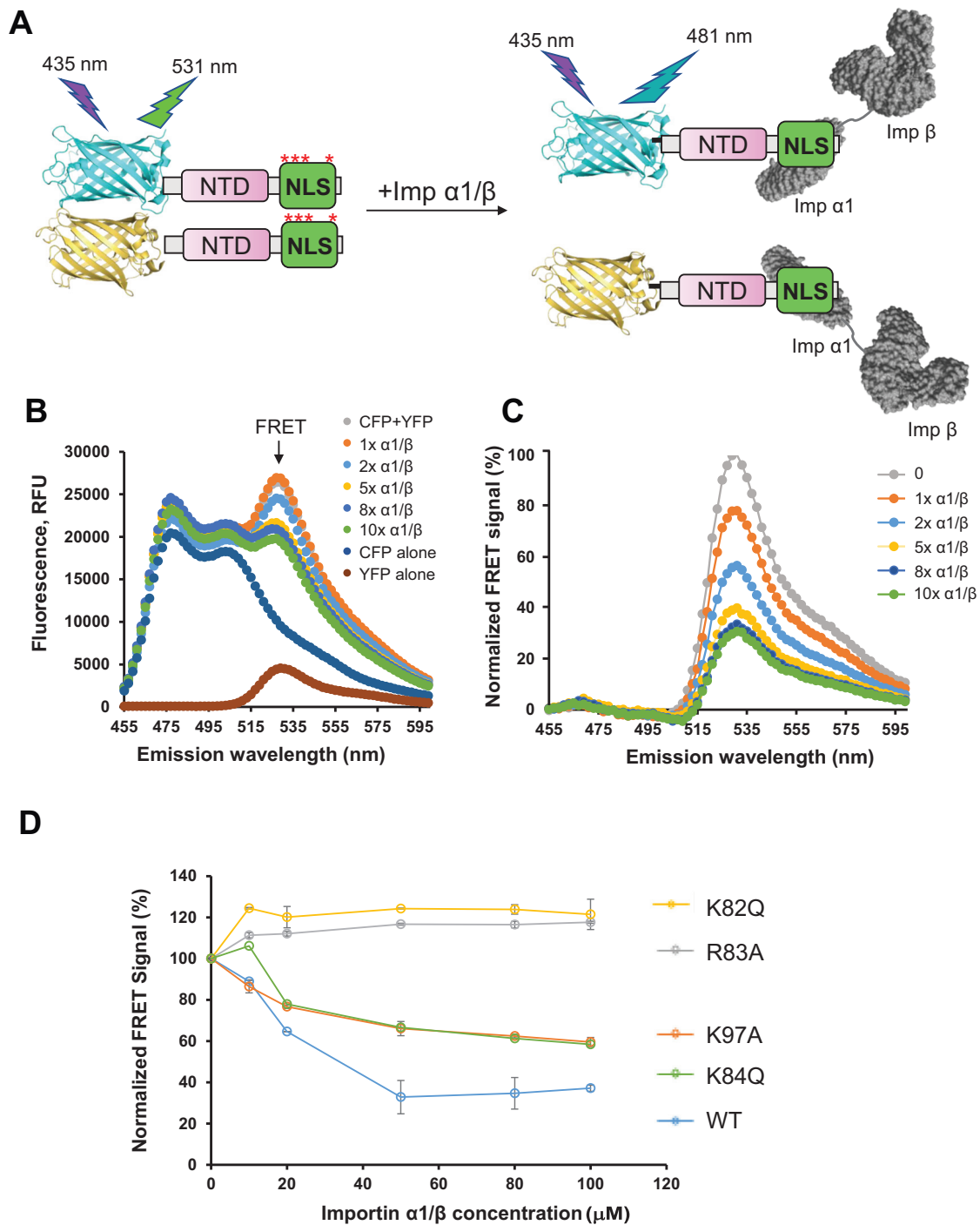


Figure 5. FRET Assay. (A) A schematic diagram of the FRET assay that was used to evaluate how mutations in the TDP-43 NLS (indicated as red asterisks) affect importin α 1/ β binding and disruption of NTD dimerization. (B) Fluorescence titration assay. An increasing quantity of purified importin α 1/ β complex between 0–100 μ M (equal to a 0–10 M excess) was titrated against 5 μ M of CFP-TDP-43-NTD-NLS and 5 μ M of YFP-TDP-43-NTD-NLS. The concentrations of importin α 1/ β shown are 0 μ M (grey), 10 μ M (1 \times , orange), 20 μ M (2 \times , light blue), 50 μ M (5 \times , yellow), 80 μ M (8 \times , dark blue), 100 μ M (10 \times , green). The fluorescence signal was recorded between 455–600 nm. (C) Quantification of normalized FRET signal at 531 nm (Y-axis) versus the importin α 1/ β concentration (X-axis). (D) Quantification of the normalized FRET signal at 531 nm (Y-axis) versus the importin α 1/ β concentration (X-axis). Lines represent different mutations/acetylation-mimetics in the TDP43 NLS. Each experimental group was independently repeated three times. The standard deviation is shown as a black bar on each data point (represented by a colored circle).

Yellow Fluorescent Protein (YFP), and CFP-TDP-43 and YFP-TDP-43 used as a FRET pair to monitor NTD dimerization (Figure 5A, left panel). When CFP-TDP-43 and YFP-TDP-43 were mixed at stoichiometric concentrations ($\sim 5 \mu\text{M}$), the engineered FRET pair produced a specific signal at 531 nm resulting from the dimerization of NTDs (Figure 5B). Previous studies demonstrated that at the concentration used in this assay, TDP-43 NTDs are dimeric with higher order assemblies formed at higher concentrations.³⁵ As the amount of the importin $\alpha 1/\beta$ complex titrated into the reaction increased (Figure 5B, C), a dramatic reduction of FRET signal at 531 nm was observed, indicating decreased energy transfer between donor and acceptor (Figure 5D). We interpret the loss of FRET signal as a disruption of TDP-43 NTD dimerization due to importin $\alpha 1/\beta$ specific association with the NLS (Figure 5A, right panel). To corroborate this idea, TDP-43 NLS makes six salt bridges, 24 H-bonds, and 214 van der Waals interactions with importin $\alpha 1$ ³⁵ versus just three salt bridges, 9 H-bonds, and 101 van der Waals interactions stabilizing the NTD dimerization interface.⁵⁰

We conducted additional experiments using various constructs with single mutations in the NLS region. We found that the K97A and K84Q mutations, while not reducing the FRET signal as much as the WT TDP-43, still led to a significant FRET decrease of 40% (Figure 5D, orange and blue line). In contrast, the negative control R83A, and even more, the acetylation mimetic K82Q consistently showed a slightly higher FRET signal at 531 nm than WT, consistent with a $\sim 25\%$ and $\sim 15\%$ rise in fluorescence emission (Figure 5D, yellow and gray lines).

Structural insights into the binding of importin $\alpha 1/\beta$ to TDP-43

In a final set of experiments, we attempted to decipher how human importin $\alpha 1/\beta$ recognize TDP-43 and whether the structure of the trimeric complex could explain the observed chaperone activity described above. At first, we purified a trimeric importin $\alpha 1/\beta$:TDP-43 complex for structural analysis. To minimize aggregation, we used a TDP-43 NTD-NLS-RRM1 (res. 1–179) (Figure 1C) that lacks the CTD and RRM2, both involved in aggregation. TDP-43 NTD-NLS-RRM1 was co-expressed in bacteria with importin $\alpha 1/\beta$, and the trimeric complex was purified in two chromatographic steps using a his-tag in importin $\alpha 1$. The importin $\alpha 1$, β and TDP-43 formed a 1:1:1 complex of ~ 170 kDa by size exclusion chromatography (SEC), as validated by sodium dodecyl-sulfate polyacrylamide gel electrophoresis (SDS-PAGE) analysis (Figure 6A). We then subjected the purified importin $\alpha 1/\beta$:TDP-43 complex to SEC coupled with small-angle X-ray scattering (SEC-SAXS)⁵¹ (Figure 6B). In a concen-

tration range between $0.5\text{--}2 \text{ mg ml}^{-1}$, the importin $\alpha 1/\beta$:TDP-43-RRM1 complex gave scattering profiles suitable for biophysical analysis. From the Guinier fits of the scattering intensities, we calculated a radius of gyration, $R_g = 53.95 \pm 0.25 \text{ \AA}$ (Figure 6C). We determined that the Volume of Correlation (V_c) mass was ~ 184.5 kDa close to ~ 174.0 kDa expected for the importin $\alpha 1/\beta$:TDP-43-RRM1 complex. The distance distribution function $P(r)$ calculated from data indicates a maximum diameter (D_{max}) of 217.2 \AA , consistent with an elongated complex (Figure 6D). We also calculated a Kratky plot of the scattering data to estimate the globularity and flexibility of the importin $\alpha 1/\beta$:TDP-43-RRM1 complex (Figure 6E). The scattering data revealed a hyperbolic region at low scattering angle indicating the presence of a globular structure. However, as the scattering angle increased, the hyperbolic region did not move to meet the X-axis but instead produced what is commensurate with a Porod plateau (Figure 6E, red bar). This region suggests the presence of flexibility within the heterotrimeric complex. We also calculated an electron density from the scattering data using DENSS⁵² that revealed an asymmetric volume similar to the number '9' (Figure 6F). We placed the solenoid structures of the importin β and $\alpha 1$:TDP-43 within the electron density generated by DENSS, and validated the proposed quaternary structure by calculating a theoretical scattering profile that fits the experimental data with a χ^2 value of 1.31 (Figure 6G). In this low-resolution model, the TDP-43 import complex is elongated with the NTD located distal from the importin β . Alternative conformations of importin β that visually fit the low-resolution SAXS density gave a higher χ^2 value (>3.5), suggesting the proposed quaternary structure shown in Figure 6F is the most likely model that fits the SAXS data. In agreement with previous SAXS data,⁵³ TDP-43 retains a bead-on-a-string topology, making high-affinity contacts with importin $\alpha 1$ NLS-binding surface.³⁵ TDP-43 NTD is over 100 \AA away from the importin β and is unlikely to contact the import receptor directly.

We also vitrified the same importin $\alpha 1/\beta$:TDP-43 complex used for SEC-SAXS (Figure 6A) and subjected it to cryogenic electron microscopy (cryo-EM) single particle analysis (SPA). We obtained a 3.7 \AA reconstruction of the complex that surprisingly only had density for the importin β solenoid bound to the N-terminal Importin β binding (IBB) domain of importin $\alpha 1$ (Figure S7A–D, Table S1). The density for the IBB-domain bound to the importin β was strong, superimposable to that observed crystallographically,⁵⁴ and all side chains could be unambiguously interpreted (Figure S7B). However, no density was seen for the importin α Armadillo-core (Arm-core) bound to TDP-43, which connects to importin β through a protease-sensitive linker.⁵⁵ We hypothesize that the importin α Arm-core:

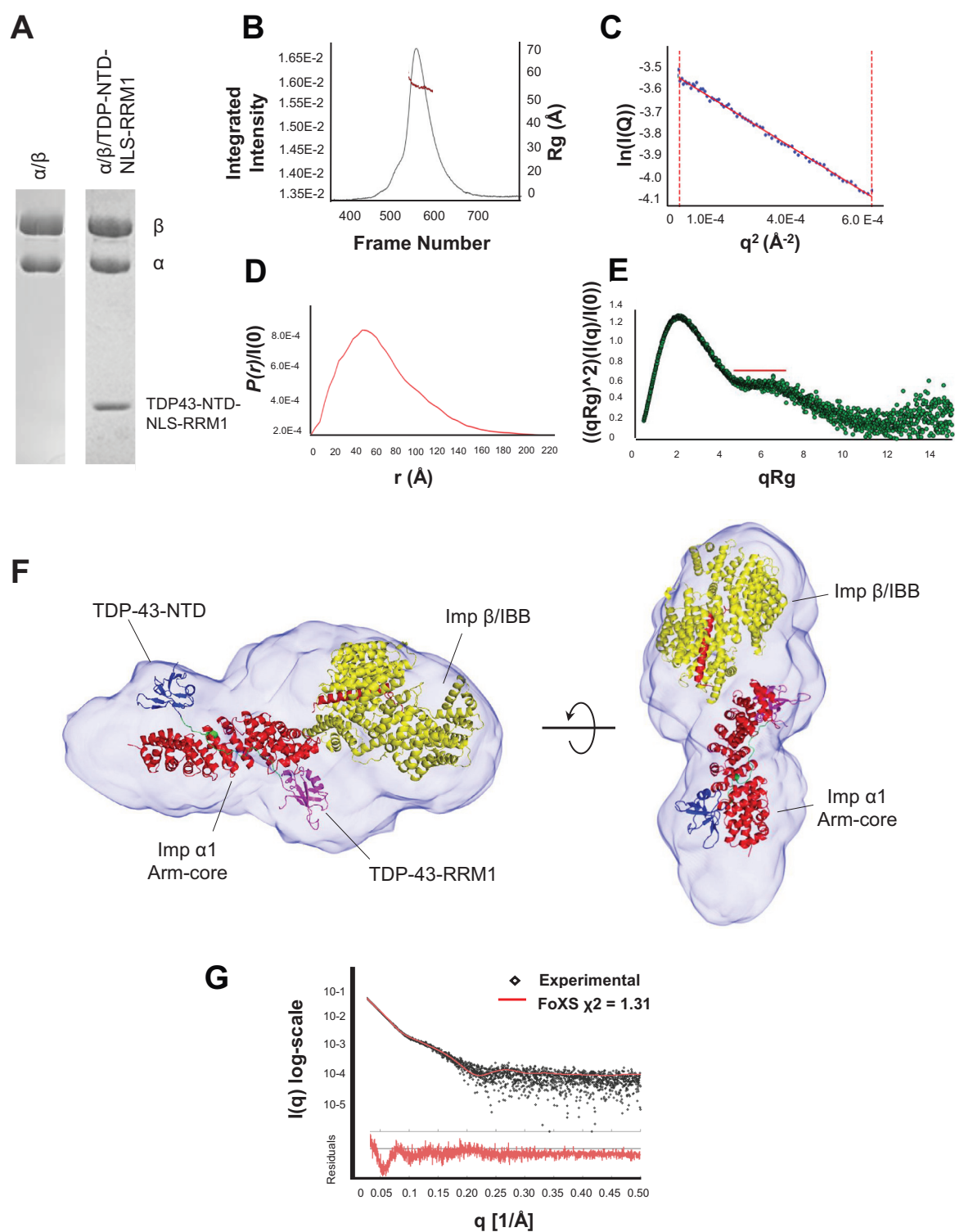


Figure 6. Solution structure of the importin α 1/ β :TDP-43 import complex. (A) SDS-Page analysis of the importin α 1/ β complex and the importin α 1/ β :TDP-43 trimeric complex used for structural studies. (B) Experimental scattering profile of the importin α 1/ β :TDP-43 complex (black trace) overlaid with Rg distribution across the scattering peak (red circles). (C) Guinier region of the intensity $I(q)$ to the scattering vector (q^2). The q_{\max} (Rg) cut-off was 1.3. (D) $P(r)$ function with D_{\max} of 217.2 Å. (E) A dimensionless Kratky plot of the scattering data. (F) Model of the importin α 1/ β :TDP-43 complex fit within the electron density (light blue) generated by DENSS. The importin α 1 is shown in red, the TDP-43 NLS in green, TDP-43-NTD in blue, and TDP-43-RRM1 in purple. (G) The comparison of the scattering profile predicted for the model to the empirical scattering of the complex produced a χ^2 value of 1.31.

TDP-43 complex exists in infinite poses relative to importin:IBB,⁵⁶ thus making it impossible to align and classify into discrete 2D classes for SPA.

Discussion

A conundrum of TDP-43 proteinopathy is that the protein rarely loses its function and aggregates because of mutations in the TDP-43 gene. TDP-43 aggregation arises due to poorly characterized cellular insults, possibly linked to Nuclear Pore Complex (NPC) dysfunction and alteration in nucleocytoplasmic transport.^{3,57–61} We previously determined that recognition of the TDP-43 NLS depends chiefly on binding to the minor NLS pocket of the importin α 1.³⁵ In this study, we sought to establish a causative relationship between PTMs reported near the P₂ of TDP-43 in ALS patients and protein mislocalization to determine if a perturbation of the TDP-43 minor NLS tract could play a dominant negative role in TDP-43 nuclear import, and hence cytoplasmic aggregation. Our data suggest that a single acetylation-mimetics at K82 disrupts two importin α 1/ β signaling aspects. On one side, it slows down TDP-43 nuclear import by weakening the NLS strength, as a cargo with a weak NLS is less likely to be imported into the cell nucleus.⁶² On the other hand, it reduces the importin α 1/ β 's ability to disrupt TDP-43 NTD dimerization, possibly leading to large aggregates. Mounting evidence suggests that NTD dimerization and the formation of larger concentration-dependent oligomers are involved in TDP-43 aggregation.^{47,48} NTD undergoes reversible oligomerization that enhances the propensity of the CTD to form amyloid-like structures^{50,63}. NTD self-association is thought to bring TDP-43 molecules closer together, enhancing the local concentration of CTDs. This intrinsically disordered portion begins the formation of amyloid-like structures,²³ and larger and larger oligomers eventually become phase-separated aggregates.

Our studies identified two distinct anti-aggregation activities in importin α 1/ β versus free importin β . The heterodimer anti-aggregation activity is strictly NLS-dependent: mutations destabilizing TDP-43 NLS binding to importin α 1 (e.g., K82Q, R83A) abolish entirely anti-aggregation activity. Instead, importin β alone, which has no detectable binding affinity for TDP-43 *in vitro*, appears to be less destabilized by mutations in the NLS. Importin β anti-aggregation activity can be explained by its highly acidic concave surface, potentially making low-affinity interaction with TDP-43 basic moieties. It is also possible that the importin β outer surface, which harbors FG-binding pockets, reduces TDP-43 aggregation *in vitro* by stabilizing FGs in TDP-43 CTD.³ Nonetheless, eukaryotic cells have low concentrations of free importin β ,⁶⁴ which suggests that the anti-aggregation activity of free importin β seen

in vitro is likely insignificant in a live cell. To rationalize how importins reduce TDP-43 aggregation, we also investigated the quaternary structure of the TDP-43 nuclear import complex using SAXS and cryo-EM. At the time scale of SAXS, we observed an elongated TDP-43 nuclear import complex with some flexibility. Our model suggests the NTD does not make direct contact with importin β . High-resolution studies by cryo-EM single particle analysis yielded a reconstruction of just importin β bound to the IBB-domain but failed to visualize the TDP-43:importin α 1 complex. We speculate that the importin α 1 Arm-core bound to TDP-43 moves at a high frequency around the importin β :IBB complex, preventing meaningful classification.⁵⁶ These structural studies suggest that importin α 1/ β chaperone activity cannot be explained by a global quaternary structure wrapping importin α 1/ β around the TDP-43 domains, akin to a chaperonin binds unfolded substrates.⁶⁵

The studies presented in this paper and the literature allow us to rationalize three distinct mechanisms by which insults in TDP-43 other than mutations lead to loss of function and aggregation, the hallmark of sporadic ALS. **First**, phosphorylation in the CTD,^{2,66,67} mainly on S379/S403/S404 and S409/S410^{68,69} decrease protein degradation and enhance TDP-43 aggregation (Figure 7A). These modifications exacerbate TDP-43's intrinsic tendency to aggregate via the prion-like CTD that ultimately results in the formation of an ultra-stable double-spiral-shaped structure characteristic of β -amyloid-like aggregates.²³ **Second**, acetylation of TDP-43 at K145 (or the acetylation-mimetic K145Q)²⁸ and possibly K136Q³⁰ reduce RNA/DNA binding affinity (Figure 7B), enhancing TDP-43 insolubility and leading to substantial loss of splicing activity.⁷⁰ The Cohen group has established endogenous models of sporadic TDP-43 acetylation at K145.²⁸ Notably, an acetylation-mimicking variant at this position recapitulates sporadic ALS, promoting the accumulation of insoluble, hyper-phosphorylated TDP-43 species that resemble pathological inclusions found in ALS and FTLD, leading to cognitive dysfunction in a mouse model. **Third**, as demonstrated in this study, an acetylation-mimetic mutation at K82 in the TDP-43 minor NLS box reduces the binding affinity for importins, slowing down nuclear import in SH-SY5Y cells and reducing importin α 1/ β chaperone-like activity towards TDP-43 aggregates *in vitro*⁴³ (Figure 7C). Thus, each of TDP-43 three domains, NTD-NLS, RRM, and CTD (Figure 7A–C) is the target of PTMs that enhance aggregation by different mechanisms. In addition, the pathogenic function of PTMs described above can be exacerbated by two cellular events promoting further TDP-43 aggregation. On one hand, hexanucleotide repeat expansion in the C9orf72 gene (found in ~50% of familial ALS cases) encodes arginine-rich dipeptide repeat proteins that bind directly to multiple

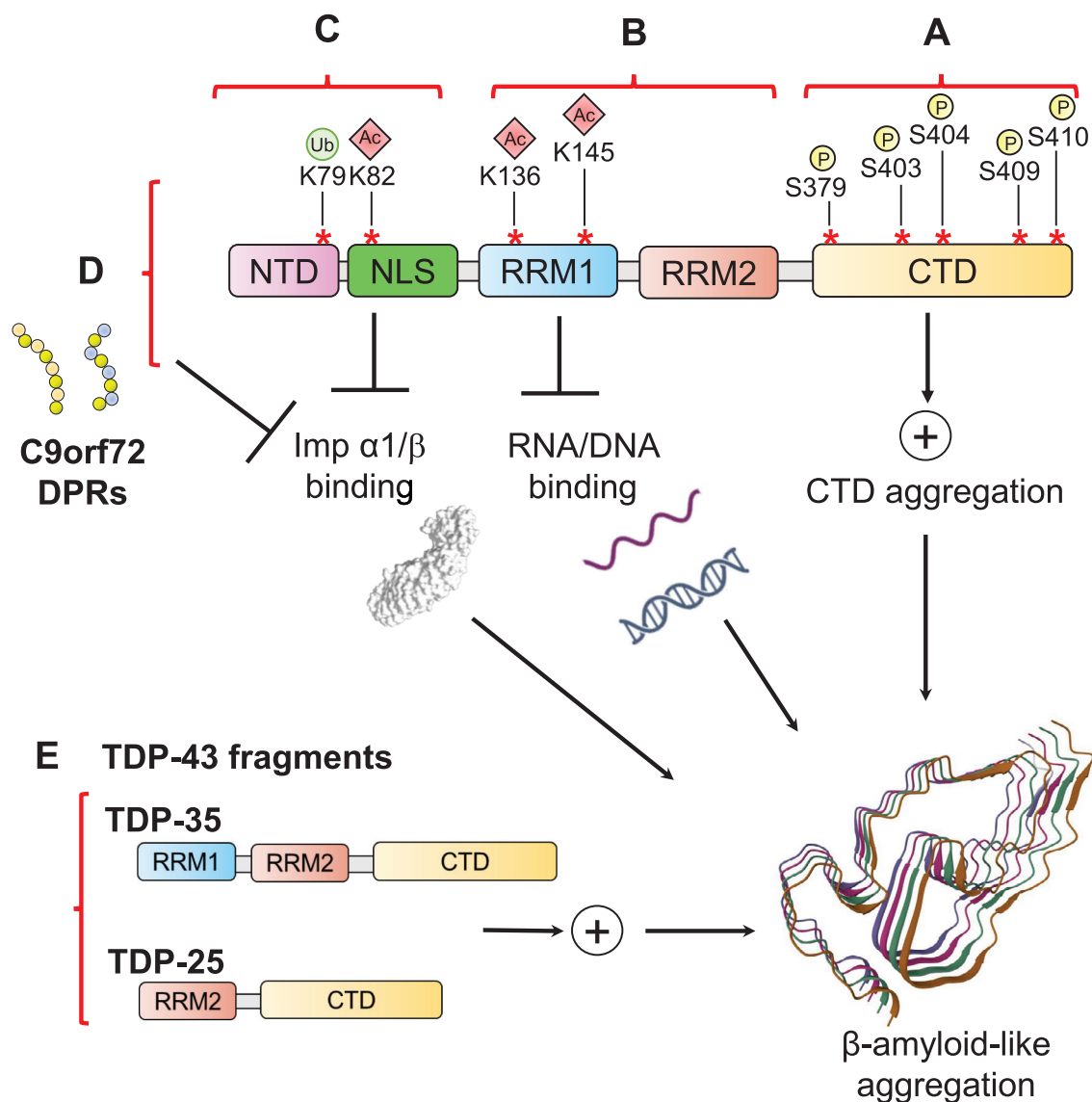


Figure 7. Model for how insults in TDP-43 lead to aggregation. (A) Phosphorylation of TDP-43 CTD at S379, S403/S404, and S409/S410 enhance aggregation. (B) Acetylation in RRMs impairs RNA binding, leading to the accumulation of insoluble TDP-43. (C) Acetylation in the NTD-NLS at K82 (and possibly ubiquitination of K79) disrupts importin α / β signaling. (D) C9orf72 DPRs impair importins function. (E) TDP-43 fragments TDP-25 and TDP-35 lacking the NLS further contribute to aggregation by making CTD-mediated contacts with WT and PTMs-modified TDP-43. Altogether, these insults cause TDP-43 aggregation and formation of β -amyloid-like aggregates.

importins and promote their insolubility and condensation, enhancing TDP-43 insolubility and phase separation^{24,25} (Figure 7D). On the other hand, TDP-43 is cleaved into smaller fragments (TDP-35 and TDP-25)⁹ lacking the NLS (Figure 7E), which functionally mimic our R83A mutation at P₂' (Figure 2B) and are expected to be strictly cytoplasmic. These C-terminal proteolytic fragments of TDP-43 increase the cytoplasmic concentration of the prion-like CTD without shuttling back and forth through the NPC. They may be significant determi-

nants in enhancing and propagating the seeding of TDP-43 aggregates.⁷¹

The scenarios described above are likely interlinked as PTMs in TDP-43 can initiate the formation of aggregates that capture both WT, truncated, and modified TDP-43, altering the kinetics of transport through the NPC and causing cytoplasmic mislocalization. This feeds a vicious cycle of a protein that continues to stall in the cytoplasm, cannot exert its housekeeping function in the nucleus, and cannot be solubilized by

importins due to impaired association. In conclusion, this paper provides *in vitro* evidence that a minor insult near TDP-43 NLS can exert a dominant negative effect on protein localization, solubility, and binding affinity for importins.

Materials and Methods

Molecular biology

The constructs WT TDP-43, NTD-NLS-RRM1, NTD-NLS-RRM1-R83A, NTD-NLS-RRM1-K97A,⁴⁹ and FL-TD-P43-MBP⁴¹ have been described previously. Briefly, FL-TDP-43 and NTD-NLS-RRM1 are cloned in pGEX-6P-1, while FL-TD-P43-MBP is cloned in pJ4M. Plasmids of eCFP and eYFP encoded at N-term of TDP-43 NTD-NLS (WT, K97A, R83A, K82Q, K84Q) mutants were synthesized by GenScript and cloned into a pET28(+)-TEV vector. Site-directed mutagenesis was used to introduce point mutations K82Q, K82A, R83A, K84Q, K84A, K97A in FL-TD-P43-MBP, NTD-NLS-RRM1, CFP-NTD-NLS, and YFP-NTD-NLS. The TDP-43-mCherry variant constructs were synthesized by VectorBuilder and cloned into their pLV vector. All constructs generated in this study were sequenced to verify the correctness of DNA sequences. [Supplementary Tables S2 and S3](#) list all the plasmids and primers used in this study.

Cell culture

SH-SY5Y, the neuroblastoma cells (ATCC), were cultured in DMEM/F12 (Gibco) supplemented with 10% fetal bovine serum (Gibco) and 1% penicillin-streptomycin (Gibco) at 37 °C with 5% CO₂. After initial transduction of SH-SY5Y by lentiviruses harboring TDP-43 variants tagged with mCherry (Vectorbuilder), cells were enriched with a BD FACS Aria cell sorter for mCherry-expressing cells. Experiments were performed within 5 passages of sorting to maintain similar levels of TDP-43 expression.

Subcellular localization studies

For fluorescence microscopy, cells were fixed with 4% PFA (Electron Microscopy Sciences) for 15 min, and permeabilized with 0.1% Triton-X-100 in 1× PBS for 15 min. Nuclei were stained with DAPI (Invitrogen), and membranes were stained with CellBrite Green (Biotium). For analysis of TDP-43 subcellular localization, cell images were acquired using a Biotek Cytation 5 multimode imaging reader. Membrane staining was used to determine the cytoplasm as a region of interest and then DAPI staining to identify the nuclear region of interest. The TDP-43 mCherry intensity in these two regions was used to calculate the percent nuclear TDP-43.

For analysis of TDP-43 cellular distribution by immunoblot analysis, SH-SY5Y cells expressing

TDP-43 variants tagged with mCherry were lysed with Thermo Subcellular Protein Fractionation Kit for cultured cells (Thermo, 78840) and processed according to the manufacturer's instructions. After one wash with ice-cold 1× PBS, ~3 million cells were lysed in 500 μL of cytoplasmic extraction buffer. For immunoblot assays 2:1:1 μL of cytoplasmic extraction buffer:nuclear extraction buffer:pellet extraction buffer were separated by Bolt™ Bis-Tris Plus Mini Protein Gels, 4–12%, 1.0 mm, WedgeWell format (Invitrogen), transferred to PVDF membranes (Invitrogen) and probed with antibodies against TDP-43 (1/1,000, ProteinTech Group). Fluorescent secondary antibodies (LiCor 800CW) were used for band detection, and the Kaleidoscope precision plus protein ladder for size estimation (BioRad). Licor imaging system and software were used to quantify protein band signal to generate distribution ratio.

Protein expression and purification

Individual pGEX-6p-1-TDP-43 NLS-RRM1 constructs were co-transformed with importin α 1/ β -pACYCDuet-1 into BL21-DE3 *E. coli* expression strain supplemented with ampicillin and chloramphenicol. Protein was expressed for 1.5 h at 30 °C with 500 μM IPTG. The heterotrimeric complex comprising TDP-43 NTD-NLS-RRM1 and the importin α 1/ β was purified in a Low-Salt Lysis buffer (20 mM Tris-HCl, pH 8.0, 75 mM NaCl, 1 mM PMSF, and 3 mM 2-mercaptoethanol) and bound to nickel agarose beads (low density, GoldBio). The complex was washed using a Low-Salt Wash buffer (20 mM Tris-HCl, pH 8.0, 50 mM NaCl, 0.1 mM PMSF, and 3 mM 2-mercaptoethanol). The GST tag was cleaved on beads through overnight incubation with PreScission protease at 4 °C. The complex was further washed with a Low-Salt buffer supplemented with 5 mM imidazole and eluted with Low-Imidazole Elution buffer (20 mM Tris-HCl, pH 8.0, 50 mM NaCl, 75 mM imidazole, 1 mM PMSF, and 3 mM 2-mercaptoethanol). These heterotrimeric complexes were further purified via size-exclusion chromatography (SEC) using a Superdex 200 16/600 preparative column. Fractions corresponding to mono-disperse TDP-43: importin α 1: β at a 1:1:1 ratio were pooled and concentrated in a 30 kDa concentrator (Vivaspin) and subjected to downstream applications. The importin α 1/ β -pACYCDuet-1 construct was transformed into BL21-DE3 *E. coli* expression strain. Proteins were expressed for 3 h at 28 °C with 500 μM IPTG. The above purification protocol was followed without subsection to protease cleavage. The untagged importin β was separated from the dimeric α 1/ β complex bound to the nickel agarose beads using a Separation buffer (20 mM Tris-HCl, pH 8.0, 250 mM MgCl₂, 150 mM NaCl, 0.1 mM PMSF, and 3 mM 2-mercaptoethanol).

The importin β was further purified and buffer-exchanged by SEC using a Superdex 200 26/600 preparative column.

For the aggregation assay, pJ4M-TDP-43-full length-TEV-MBP-his-tagged wild type and mutant (K82Q, R83A, K84Q, K97A) constructs each were transformed into BL21-DE3 *E. coli* expression strain. Proteins were expressed for 4 h at 28 °C with 500 μ M IPTG. The TDP-43 with MBP-tagged full-length proteins were lysed in Lysis buffer (20 mM Tris-HCl, pH 8.0, 150 mM NaCl, 0.1% sarcosine, 1 mM PMSF, and 3 mM 2-mercaptoethanol) and bound to low-density nickel agarose beads. The proteins were washed with a High-Salt Wash buffer (20 mM Tris-HCl, pH 8.0, 600 mM NaCl, 0.1 mM PMSF and 3 mM 2-mercaptoethanol) containing 5 mM imidazole and 10 mM imidazole and eluted with High-Imidazole Elution buffer (20 mM Tris-HCl, pH 8.0, 150 mM imidazole, 150 mM NaCl, 0.1 mM PMSF, and 3 mM 2-mercaptoethanol). The proteins were further purified, and buffer exchanged to Gel Filtration buffer (20 mM HEPES pH 7.4, 150 mM NaCl, 0.1 mM PMSF and 3 mM 2-mercaptoethanol) by SEC using a Superdex 200 16:600 preparative column.

Fusion proteins for the FRET assay were expressed for 3 h at 30 °C with 500 μ M IPTG. The CFP- and YFP-tagged TDPs were purified in a Low-Salt Lysis buffer (20 mM Tris-HCl, pH 8.0, 50 mM NaCl, 1 mM PMSF, and 3 mM 2-mercaptoethanol) and bound to low-density nickel beads and washed using a Low-Salt Wash buffer (20 mM Tris-HCl, pH 8.0, 50 mM NaCl, 0.1 mM PMSF, and 3 mM 2-mercaptoethanol). The proteins were eluted with High-Imidazole Elution buffer (20 mM Tris-HCl, pH 8.0, 150 mM imidazole, 150 mM NaCl, 0.1 mM PMSF, and 3 mM 2-mercaptoethanol). All proteins were further purified by SEC using a Superdex 200 16:600 preparative column. SEC was conducted using a BioRad NGC single wavelength FPLC unit for all purifications described in this paper. BioRad provided ChromLab software to facilitate the visualization and analysis of chromatograms.

In cellulo pull-down assays

Plasmids encoding pGEX-6p-1-TDP-43 NTD-NLS-RRM1 (WT, K97A, R83A, K82Q, K84Q, K82A, K84A) mutants were co-expressed in *E. coli* BL21-DE3 expression strain with the pETDuet-1 plasmid expressing the importin α 1/ β . Protein was expressed for 1.5 h at 30 °C with 500 μ M IPTG. Pre- and post-induction optical densities were measured for each co-transformant to ensure a similar growth rate across all cultures. Trimeric complexes were purified as previously described for the importin α 1/ β complex and eluted from equal volumes of low-density nickel beads. Eluates were analyzed by SDS-PAGE gel. Volumes corresponding to an equal mass of the

importin α 1 were loaded onto a 13.7% SDS-PAGE gel alongside molecular weight markers. SDS-PAGE gels were run in triplicate ($n = 3$), and the average ratio of GST-TDP-43 NTD-NLS-RRM1 to the importin α 1 band intensity was calculated for each construct through densitometry using ImageJ.⁷² We employed a two-tailed Student's T-test assuming unequal variance to determine statistical significance between the means of the control and experimental pull-downs. The alpha parameter had to be outside the 99th percentile for statistical significance ($p < 0.001$, indicated by ***). Error bars indicate the standard deviation of the mean.

Turbidity assay and visualization of aggregates by light microscopy

Turbidity was used to assess spontaneous aggregation by measuring absorbance at 395 nm by TECAN Spark plate reader (TECAN). The TDP-43 aggregation was also confirmed by 6 μ L of protein under 100 \times magnification microscope (Leica DMI8) at different time points. TDP-43 (10 μ M) aggregation was initiated by adding TEV protease that cleaves the affinity tag (MBP) on the C-end of the TDP-43-full length-MBP proteins. TDP-43 aggregation is monitored by continuous reading at 395 nm (OD395), which we measure every minute using a TECAN with a humidity control chamber at 37 °C for 50 min. The TDP-43 aggregates were inspected using a conventional light microscope (Leica DMI8, 100 \times magnification) after 50 mins. For Anti-aggregation, the importin α 1/ β complex (25 μ M) was pre-incubated with TDP-43 before adding TEV protease and following the same measurement previously described.

FRET assay

Purified TDP-43 CFP-NTD-NLS and NTD-NLS-YFP proteins were concentrated to about 100 μ M range while the imp α 1/ β heterodimer was concentrated to about 150 μ M. For the assay, 5 μ M ECFP and 5 μ M EYFP with the same TDP-43 mutants were pre-incubated for 1 h at 4C in the well of a 96-well Blackwell plate. After 1 h, 10–100 μ M of importin α 1/ β or buffer (as control) were added to the TDP-43 and incubated for another 2 h. 5 μ M CFP-TDPs only and 5 μ M YFP-TDPs were also included for reference. Fluorescence recordings were performed with a TECAN Spark plate reader. A fixed excitation wavelength of 435 nm with a bandwidth of 7.5 nm was employed for the entire assay. Emission wavelengths of 483 nm and 530 nm were consistently recorded during the assay. In the titration assay for importin α 1/ β , emission wavelengths from 455 nm to 600 nm were continuously recorded. All FRET assays were conducted at room temperature, approximately 23 °C. FRET normalization for each group was calculated using the formula:

FRET normalization

$$= \left(\left(\frac{OD530(\text{sample}) \times OD483(\text{CFP} - \text{YFP})}{OD483(\text{sample})} \right) - OD530(\text{CFP}) - OD530(\text{YFP}) \right) \times 100\%$$

Size exclusion chromatography coupled to small-angle X-ray diffraction (SEC-SAXS)

Importin α 1/ β :TDP-43-NTD-NLS-RRM1 complex was analyzed at the Cornell High Energy Synchrotron Source (CHESS) beamline G1 at Cornell University in Ithaca, NY. The complex was first separated on a Superdex 200 16:600 column and then subjected to X-ray studies. Small-angle diffraction data was collected and subsequently processed using the RAW software package (version 2.1.1),⁷³ including plug-ins from ATSAS.⁷⁴ Sample peak intensities were normalized to a region of the scattering baseline that satisfied the following conditions: 1. The selected baseline did not include any individual frames that differed significantly from the average intensity, and 2. The selected baseline produced a distribution of radii of gyration that included a Guinier region. From the Guinier region, the molecular mass of each complex was predicted, and a P(r) plot was generated. P(r) plots corresponding to each complex were submitted to the DENsity from Solution Scattering (DENSS)⁵² plug-in to generate low-resolution electron densities. We modeled the TDP-43 NTD-NLS and NLS-RRM1 bound to Δ IBB-importin α 1 using available crystal structures of TDP-43 NTD (PDB: 5MDI) and TDP-43 RRM1 (PDB: 4BS2), mouse importin α 1 (PDB: 1Y2A) and importin β (PDB: 1QGK). These complexes were fit into the DENSS density and refined against the low-resolution SAXS density using the *fit-into-map* command in Chimera.⁷⁵ The scattering profiles of these models were compared to the empirically observed scattering data using the FoXS server,⁷⁶ which generated a predicted-to-observed χ^2 value in each case.

Vitrification and Cryo-EM data collection and single particle analysis

2 μ L of the heterotrimeric importin α 1/ β :TDP-43-NTD-NLS-RRM1 complex was applied to a 200-mesh copper Quantifoil R1.2/1.3 holey carbon grid (EMS) that had been negatively glow-discharged for 60 sec at 15 mA in easiGlow (PELCO). All grids were blotted for 5 sec at blot force 5 and frozen in liquid ethane using Vitrobot Mark IV (FEI). Micrographs were pre-screened on 200 kV Glacios equipped with a Falcon4 detector at Thomas Jefferson University. EPU software was used for data collection using accurate positioning mode. For high-resolution data collection, micrographs were collected on a Titan Krios microscope operated at 300 kV and equipped with

a K3 direct electron detector camera (Gatan) at the National Cryo-EM Facility. A total of 6,400 movies were collected. All cryo-EM data collection statistics are in Table S1. The Fourier Shell Correlation (FSC) resolution curve is in Figure S7C. All movies were imported and analyzed by cryo-SPARC,⁷⁷ including patched motion-correction, patched CTF (contract Transfer Function) estimation, exposure curation, particle picking and curating, 2D and hetero 3D classification, homogeneous refinement with CTF and defocus refinement options, and post-processing on a GPU cluster at Thomas Jefferson University. The density map of IBB bound the importin β was sharpened using *phenix.auto_sharpen*.⁷⁸ The model of IBB bound the importin β was subjected to several rounds of rigid-, real-space, and B-factor refinement using *phenix.real_space_refinement*.⁷⁹ The final model was validated using MolProbity.⁸⁰

CRedit authorship contribution statement

Ying-Hui Ko: Writing – review & editing, Writing – original draft, Validation, Methodology, Formal analysis, Data curation, Conceptualization. **Ravi K. Lokareddy:** Writing – review & editing, Conceptualization. **Steven G. Doll:** Formal analysis. **Daniel P. Yeggoni:** Data curation. **Amandeep Girdhar:** Methodology. **Ian Mawn:** Formal analysis, Data curation. **Joseph R. Klim:** Formal analysis, Data curation. **Noreen F. Rizvi:** Project administration, Formal analysis, Conceptualization. **Rachel Meyers:** Project administration, Conceptualization. **Richard E. Gillilan:** Data curation. **Lin Guo:** Writing – review & editing, Supervision, Methodology, Formal analysis, Data curation, Conceptualization. **Gino Cingolani:** Writing – review & editing, Writing – original draft, Validation, Supervision, Methodology, Investigation, Funding acquisition, Formal analysis, Conceptualization.

DATA AVAILABILITY

Data will be made available on request.

DECLARATION OF COMPETING INTEREST

The authors declare that they have no known competing financial interests or personal relationships that could have appeared to influence the work reported in this paper.

Acknowledgments

This work was supported by NIH grants R35 GM140733, R21 NS128396, S10 OD017987, and S10 OD023479 to G.C., and by Dr. Ralph and Marian Falk Medical Research Trust, and NIH grants R35GM138109 and RF1NS121143 to L.G.

Research in this publication includes work carried out at MacCHESS, which is supported by the NSF grant DMR-1829070, and the MacCHESS resource is supported by the NIH grant P30 GM124166-01A1 and NYSTAR. This research was, in part, supported by the National Cancer Institute's National Cryo-EM Facility (NCEF) at the Frederick National Laboratory for Cancer Research under contract HSSN261200800001E.

Appendix A. Supplementary material

Supplementary material to this article can be found online at <https://doi.org/10.1016/j.jmb.2024.168751>.

Received 18 May 2024;

Accepted 18 August 2024;

Available online 22 August 2024

Keywords:

TDP-43;
ALS;
importin α 1;
importin β ;
nuclear localization signal

Abbreviations:

TDP-43, TAR-DNA binding protein of 43 kDa; ALS, amyotrophic lateral sclerosis; FTD, frontotemporal lobar degeneration; NTD, N-terminal domain; NLS, Nuclear Localization Signal; RRM, RNA binding module; CTD, C-terminal domain; PTM, post-translational modifications; Imp, importin; IBB, Importin β binding domain; cryo-EM, cryogenic electron microscopy; SEC, size exclusion chromatography; SPA, single-particle analysis; CFP, Cyan Fluorescent Protein; YFP, Yellow Fluorescent Protein; FRET, fluorescence resonance energy transfer; CC, correlation coefficient; M.W., molecular weight; SDS-PAGE, sodium dodecyl sulfate–polyacrylamide gel electrophoresis; SAXS, small angle X-ray scattering

References

- Andersen, P.M., Al-Chalabi, A., (2011). Clinical genetics of amyotrophic lateral sclerosis: what do we really know? *Nature Rev. Neurol.* **7**, 603–615.
- François-Moutal, L., Perez-Miller, S., Scott, D.D., Miranda, V.G., Mollasalehi, N., Khanna, M., (2019). Structural insights into TDP-43 and effects of post-translational modifications. *Front. Mol. Neurosci.* **12**, 301.
- Doll, S.G., Cingolani, G., (2022). Importin alpha/beta and the tug of war to keep TDP-43 in solution: quo vadis? *Bioessays* **44**, e2200181.
- Neumann, M., Sampathu, D.M., Kwong, L.K., Truax, A.C., Micsenyi, M.C., Chou, T.T., et al., (2006). Ubiquitinated TDP-43 in frontotemporal lobar degeneration and amyotrophic lateral sclerosis. *Science* **314**, 130–133.
- Masrori, P., Van Damme, P., (2020). Amyotrophic lateral sclerosis: a clinical review. *Eur. J. Neurol.* **27**, 1918–1929.
- Xu, Z., Yang, C., (2014). TDP-43-The key to understanding amyotrophic lateral sclerosis. *Rare Dis.* **2**, e944443.
- Jo, M., Lee, S., Jeon, Y.M., Kim, S., Kwon, Y., Kim, H.J., (2020). The role of TDP-43 propagation in neurodegenerative diseases: integrating insights from clinical and experimental studies. *Exp. Mol. Med.* **52**, 1652–1662.
- Prasad, A., Bharathi, V., Sivalingam, V., Girdhar, A., Patel, B.K., (2019). Molecular mechanisms of TDP-43 misfolding and pathology in amyotrophic lateral sclerosis. *Front. Mol. Neurosci.* **12**, 25.
- Chhangani, D., Martin-Pena, A., Rincon-Limas, D.E., (2021). Molecular, functional, and pathological aspects of TDP-43 fragmentation. *Iscience* **24**, 102459.
- Sun, Y., Chakrabarty, A., (2017). Phase to phase with TDP-43. *Biochemistry* **56**, 809–823.
- Smethurst, P., Sidle, K.C., Hardy, J., (2015). Review: Prion-like mechanisms of transactive response DNA binding protein of 43 kDa (TDP-43) in amyotrophic lateral sclerosis (ALS). *Neuropathol. Appl. Neurobiol.* **41**, 578–597.
- Hergesheimer, R.C., Chami, A.A., de Assis, D.R., Vourc'h, P., Andres, C.R., Corcia, P., et al., (2019). The debated toxic role of aggregated TDP-43 in amyotrophic lateral sclerosis: a resolution in sight? *Brain* **142**, 1176–1194.
- Buratti, E., Baralle, F.E., (2009). The molecular links between TDP-43 dysfunction and neurodegeneration. *Adv. Genet.* **66**, 1–34.
- Buratti, E., (2018). TDP-43 post-translational modifications in health and disease. *Expert Opin. Ther. Targets* **22**, 279–293.
- Wang, H.Y., Wang, I.F., Bose, J., Shen, C.K., (2004). Structural diversity and functional implications of the eukaryotic TDP gene family. *Genomics* **83**, 130–139.
- Donde, A., Sun, M., Ling, J.P., Braunstein, K.E., Pang, B., Wen, X., et al., (2019). Splicing repression is a major function of TDP-43 in motor neurons. *Acta Neuropathol.* **138**, 813–826.
- Ling, J.P., Pletnikova, O., Troncoso, J.C., Wong, P.C., (2015). TDP-43 repression of nonconserved cryptic exons is compromised in ALS-FTD. *Science* **349**, 650–655.
- Melamed, Z., Lopez-Erauskin, J., Baughn, M.W., Zhang, O., Drenner, K., Sun, Y., et al., (2019). Premature polyadenylation-mediated loss of stathmin-2 is a hallmark of TDP-43-dependent neurodegeneration. *Nature Neurosci.* **22**, 180–190.
- Klim, J.R., Williams, L.A., Limone, F., Guerra San Juan, I., Davis-Dusenbery, B.N., Mordes, D.A., et al., (2019). ALS-implicated protein TDP-43 sustains levels of STMN2, a mediator of motor neuron growth and repair. *Nature Neurosci.* **22**, 167–179.
- Prudencio, M., Humphrey, J., Pickles, S., Brown, A.L., Hill, S.E., Kachergus, J.M., et al., (2020). Truncated stathmin-2 is a marker of TDP-43 pathology in frontotemporal dementia. *J. Clin. Invest.* **130**, 6080–6092.
- Ma, X.R., Prudencio, M., Koike, Y., Vatsavayai, S.C., Kim, G., Harbinski, F., et al., (2022). TDP-43 represses cryptic exon inclusion in the FTD-ALS gene UNC13A. *Nature* **603**, 124–130.
- Pooryasin, A., Maglione, M., Schubert, M., Matkovic-Rachid, T., Hasheminasab, S.M., Pech, U., et al., (2021). Unc13A and Unc13B contribute to the decoding of distinct sensory information in Drosophila. *Nature Commun.* **12**, 1932.

23. Arseni, D., Hasegawa, M., Murzin, A.G., Kametani, F., Arai, M., Yoshida, M., et al., (2022). Structure of pathological TDP-43 filaments from ALS with FTLD. *Nature* **601**, 139–143.
24. Hutten, S., Usluer, S., Bourgeois, B., Simonetti, F., Odeh, H.M., Fare, C.M., et al., (2020). Nuclear import receptors directly bind to arginine-rich dipeptide repeat proteins and suppress their pathological interactions. *Cell Rep.* **33**, 108538.
25. McGoldrick, P., Robertson, J., (2023). Unraveling the impact of disrupted nucleocytoplasmic transport systems in C9orf72-associated ALS. *Front. Cell. Neurosci.* **17**, 1247297.
26. Eck, R.J., Kraemer, B.C., Liachko, N.F., (2021). Regulation of TDP-43 phosphorylation in aging and disease. *Geroscience.* **43**, 1605–1614.
27. Hornbeck, P.V., Zhang, B., Murray, B., Kornhauser, J.M., Latham, V., Skrzypek, E., (2015). PhosphoSitePlus, 2014: mutations, PTMs and recalibrations. *Nucleic Acids Res.* **43**, D512–D520.
28. Cohen, T.J., Hwang, A.W., Restrepo, C.R., Yuan, C.X., Trojanowski, J.Q., Lee, V.M., (2015). An acetylation switch controls TDP-43 function and aggregation propensity. *Nature Commun.* **6**, 5845.
29. Kametani, F., Obi, T., Shishido, T., Akatsu, H., Murayama, S., Saito, Y., et al., (2016). Mass spectrometric analysis of accumulated TDP-43 in amyotrophic lateral sclerosis brains. *Sci. Rep.* **6**, 23281.
30. Garcia Morato, J., Hans, F., von Zweydford, F., Feederle, R., Elsasser, S.J., Skodras, A.A., et al., (2022). Sirtuin-1 sensitive lysine-136 acetylation drives phase separation and pathological aggregation of TDP-43. *Nature Commun.* **13**, 1223.
31. Khosravi, B., LaClair, K.D., Riemenschneider, H., Zhou, Q., Frottin, F., Mareljic, N., et al., (2020). Cell-to-cell transmission of C9orf72 poly-(Gly-Ala) triggers key features of ALS/FTD. *EMBO J.* **39**, e102811.
32. Winton, M.J., Van Deerlin, V.M., Kwong, L.K., Yuan, W., Wood, E.M., Yu, C.E., et al., (2008). A90V TDP-43 variant results in the aberrant localization of TDP-43 in vitro. *FEBS Lett.* **582**, 2252–2256.
33. Kametani, F., Nonaka, T., Suzuki, T., Arai, T., Dohmae, N., Akiyama, H., et al., (2009). Identification of casein kinase-1 phosphorylation sites on TDP-43. *Biochem. Biophys. Res. Commun.* **382**, 405–409.
34. Nonaka, T., Suzuki, G., Tanaka, Y., Kametani, F., Hirai, S., Okado, H., et al., (2016). Phosphorylation of TAR DNA-binding protein of 43 kDa (TDP-43) by truncated casein kinase 1delta triggers mislocalization and accumulation of TDP-43. *J. Biol. Chem.* **291**, 5473–5483.
35. Doll, S.G., Meshkin, H., Bryer, A.J., Li, F., Ko, Y.H., Lokareddy, R.K., et al., (2022). Recognition of the TDP-43 nuclear localization signal by importin α 1/ β . *Cell Rep.* **39**, 111007.
36. Grujic da Silva, L.A., Simonetti, F., Hutten, S., Riemenschneider, H., Sternburg, E.L., Pietrek, L.M., et al., (2022). Disease-linked TDP-43 hyperphosphorylation suppresses TDP-43 condensation and aggregation. *EMBO J.* **41**, e108443.
37. Hasegawa, M., Arai, T., Nonaka, T., Kametani, F., Yoshida, M., Hashizume, Y., et al., (2008). Phosphorylated TDP-43 in frontotemporal lobar degeneration and amyotrophic lateral sclerosis. *Ann. Neurol.* **64**, 60–70.
38. Wobst, H.J., Delsing, L., Brandon, N.J., Moss, S.J., (2017). Truncation of the TAR DNA-binding protein 43 is not a prerequisite for cytoplasmic relocalization, and is suppressed by caspase inhibition and by introduction of the A90V sequence variant. *PLoS One* **12**, e0177181.
39. Ederle, H., Dormann, D., (2017). TDP-43 and FUS en route from the nucleus to the cytoplasm. *FEBS Lett.* **591**, 1489–1507.
40. Winton, M.J., Igaz, L.M., Wong, M.M., Kwong, L.K., Trojanowski, J.Q., Lee, V.M., (2008). Disturbance of nuclear and cytoplasmic TAR DNA-binding protein (TDP-43) induces disease-like redistribution, sequestration, and aggregate formation. *J. Biol. Chem.* **283**, 13302–13309.
41. Ayala, Y.M., Zago, P., D'Ambrogio, A., Xu, Y.F., Petrucelli, L., Buratti, E., et al., (2008). Structural determinants of the cellular localization and shuttling of TDP-43. *J. Cell Sci.* **121**, 3778–3785.
42. Pinarbasi, E.S., Cağatay, T., Fung, H.Y.J., Li, Y.C., Chook, Y.M., Thomas, P.J., (2018). Active nuclear import and passive nuclear export are the primary determinants of TDP-43 localization. *Sci. Rep.* **8**, 7083.
43. Guo, L., Kim, H.J., Wang, H., Monaghan, J., Freyermuth, F., Sung, J.C., et al., (2018). Nuclear-import receptors reverse aberrant phase transitions of RNA-binding proteins with prion-like domains. *Cell* **173**, 677–692.e20.
44. Cook, C.N., Wu, Y., Odeh, H.M., Gendron, T.F., Jansen-West, K., Del Rosso, G., et al., (2020). C9orf72 poly(GR) aggregation induces TDP-43 proteinopathy. *Sci. Transl. Med.*, 12.
45. Jiang, L.L., Xue, W., Hong, J.Y., Zhang, J.T., Li, M.J., Yu, S.N., et al., (2017). The N-terminal dimerization is required for TDP-43 splicing activity. *Sci. Rep.* **7**, 6196.
46. Mompean, M., Romano, V., Pantoja-Uceda, D., Stuardi, C., Baralle, F.E., Buratti, E., et al., (2017). Point mutations in the N-terminal domain of transactive response DNA-binding protein 43 kDa (TDP-43) compromise its stability, dimerization, and functions. *J. Biol. Chem.* **292**, 11992–12006.
47. Shiina, Y., Arima, K., Tabunoki, H., Satoh, J., (2010). TDP-43 dimerizes in human cells in culture. *Cell. Mol. Neurobiol.* **30**, 641–652.
48. Wang, Y.T., Kuo, P.H., Chiang, C.H., Liang, J.R., Chen, Y. R., Wang, S., et al., (2013). The truncated C-terminal RNA recognition motif of TDP-43 protein plays a key role in forming proteinaceous aggregates. *J. Biol. Chem.* **288**, 9049–9057.
49. Chang, C.K., Wu, T.H., Wu, C.Y., Chiang, M.H., Toh, E.K., Hsu, Y.C., et al., (2012). The N-terminus of TDP-43 promotes its oligomerization and enhances DNA binding affinity. *Biochem. Biophys. Res. Commun.* **425**, 219–224.
50. Wang, A., Conicella, A.E., Schmidt, H.B., Martin, E.W., Rhoads, S.N., Reeb, A.N., et al., (2018). A single N-terminal phosphomimic disrupts TDP-43 polymerization, phase separation, and RNA splicing. *EMBO J.* **37**
51. Acerbo, A.S., Cook, M.J., Gillilan, R.E., (2015). Upgrade of MacCHESS facility for X-ray scattering of biological macromolecules in solution. *J. Synchrotron Radiat.* **22**, 180–186.
52. Grant, T.D., (2018). Ab initio electron density determination directly from solution scattering data. *Nature Methods* **15**, 191–193.
53. Wright, G.S.A., Watanabe, T.F., Ampornpanai, K., Plotkin, S.S., Cashman, N.R., Antonyuk, S.V., et al., (2020). Purification and structural characterization of aggregation-

- prone human TDP-43 involved in neurodegenerative diseases. *iScience* **23**, 101159.
54. Cingolani, G., Petosa, C., Weis, K., Muller, C.W., (1999). Structure of importin-beta bound to the IBB domain of importin-alpha. *Nature* **399**, 221–229.
 55. Cingolani, G., Lashuel, H.A., Gerace, L., Muller, C.W., (2000). Nuclear import factors importin alpha and importin beta undergo mutually induced conformational changes upon association. *FEBS Lett.* **484**, 291–298.
 56. Yang, R., Ko, Y.H., Li, F., Lokareddy, R.K., Hou, C.D., Kim, C., et al., (2024). Structural basis for nuclear import of hepatitis B virus (HBV) nucleocapsid core. *Sci. Adv.* **10**, eadi7606.
 57. Zhang, K., Grima, J.C., Rothstein, J.D., Lloyd, T.E., (2016). Nucleocytoplasmic transport in C9orf72-mediated ALS/FTD. *Nucleus* **7**, 132–137.
 58. Suk, T.R., Rousseaux, M.W.C., (2020). The role of TDP-43 mislocalization in amyotrophic lateral sclerosis. *Mol. Neurodegener.* **15**, 45.
 59. Chou, C.C., Zhang, Y., Umoh, M.E., Vaughan, S.W., Lorenzini, I., Liu, F., et al., (2018). TDP-43 pathology disrupts nuclear pore complexes and nucleocytoplasmic transport in ALS/FTD. *Nature Neurosci.* **21**, 228–239.
 60. Zhang, K., Daigle, J.G., Cunningham, K.M., Coyne, A.N., Ruan, K., Grima, J.C., et al., (2018). Stress granule assembly disrupts nucleocytoplasmic transport. *Cell* **173**, 958–971.e17.
 61. Hayes, L.R., Duan, L., Bowen, K., Kalab, P., Rothstein, J. D., (2020). C9orf72 arginine-rich dipeptide repeat proteins disrupt karyopherin-mediated nuclear import. *Elife* **9**
 62. Fanara, P., Hodel, M.R., Corbett, A.H., Hodel, A.E., (2000). Quantitative analysis of nuclear localization signal (NLS)-importin alpha interaction through fluorescence depolarization. Evidence for auto-inhibitory regulation of NLS binding. *J. Biol. Chem.* **275**, 21218–21223.
 63. Tsoi, P.S., Choi, K.J., Leonard, P.G., Sizovs, A., Moosa, M. M., MacKenzie, K.R., et al., (2017). The N-terminal domain of ALS-linked TDP-43 assembles without misfolding. *Angew. Chem. Int. Ed. Engl.* **56**, 12590–12593.
 64. Riddick, G., Macara, I.G., (2005). A systems analysis of importin-{alpha}-{beta} mediated nuclear protein import. *J. Cell Biol.* **168**, 1027–1038.
 65. Stan, G., Lorimer, G.H., Thirumalai, D., (2022). Friends in need: How chaperonins recognize and remodel proteins that require folding assistance. *Front. Mol. Biosci.* **9**, 1071168.
 66. Berning, B.A., Walker, A.K., (2019). The pathobiology of TDP-43 C-terminal fragments in ALS and FTL. *Front. Neurosci.* **13**, 335.
 67. Farina, S., Esposito, F., Battistoni, M., Biamonti, G., Francia, S., (2021). Post-translational modifications modulate proteinopathies of TDP-43, FUS and hnRNP-A/B in amyotrophic lateral sclerosis. *Front. Mol. Biosci.* **8**, 693325.
 68. Neumann, M., Kwong, L.K., Lee, E.B., Kremmer, E., Flatley, A., Xu, Y., et al., (2009). Phosphorylation of S409/410 of TDP-43 is a consistent feature in all sporadic and familial forms of TDP-43 proteinopathies. *Acta Neuropathol.* **117**, 137–149.
 69. Neumann, M., Frick, P., Paron, F., Kosten, J., Buratti, E., Mackenzie, I.R., (2020). Antibody against TDP-43 phosphorylated at serine 375 suggests conformational differences of TDP-43 aggregates among FTL. *Acta Neuropathol.* **140**, 645–658.
 70. Wang, P., Wander, C.M., Yuan, C.X., Bereman, M.S., Cohen, T.J., (2017). Acetylation-induced TDP-43 pathology is suppressed by an HSF1-dependent chaperone program. *Nature Commun.* **8**, 82.
 71. Kumar, S.T., Nazarov, S., Porta, S., Maharjan, N., Cendrowska, U., Kabani, M., et al., (2023). Seeding the aggregation of TDP-43 requires post-fibrillation proteolytic cleavage. *Nature Neurosci.* **26**, 983–996.
 72. Abramoff, M.D., Magelhaes, P.J., Ram, S.J., (2004). Image processing with ImageJ. *Biophotonics Int.* **11**, 36–42.
 73. Hopkins, J.B., Gillilan, R.E., Skou, S., (2017). BioXTAS RAW: improvements to a free open-source program for small-angle X-ray scattering data reduction and analysis. *J. Appl. Cryst.* **50**, 1545–1553.
 74. Franke, D., Petoukhov, M.V., Konarev, P.V., Panjkovich, A., Tuukkanen, A., Mertens, H.D.T., et al., (2017). ATSAS 2.8: a comprehensive data analysis suite for small-angle scattering from macromolecular solutions. *J. Appl. Cryst.* **50**, 1212–1225.
 75. Pettersen, E.F., Goddard, T.D., Huang, C.C., Couch, G.S., Greenblatt, D.M., Meng, E.C., et al., (2004). UCSF Chimera—a visualization system for exploratory research and analysis. *J. Comput. Chem.* **25**, 1605–1612.
 76. Schneidman-Duhovny, D., Hammel, M., Sali, A., (2010). FoXS: a web server for rapid computation and fitting of SAXS profiles. *Nucleic Acids Res.* **38**, W540–W544.
 77. Punjani, A., Rubinstein, J.L., Fleet, D.J., Brubaker, M.A., (2017). cryoSPARC: algorithms for rapid unsupervised cryo-EM structure determination. *Nature Methods* **14**, 290–296.
 78. Yu, I., Nguyen, L., Avaylon, J., Wang, K., Lai, M., Zhou, Z. H., (2018). Building atomic models based on near atomic resolution cryoEM maps with existing tools. *J. Struct. Biol.* **204**, 313–318.
 79. Afonine, P.V., Poon, B.K., Read, R.J., Sobolev, O.V., Terwilliger, T.C., Urzhumtsev, A., et al., (2018). Real-space refinement in PHENIX for cryo-EM and crystallography. *Acta Crystallogr. D Struct. Biol.* **74**, 531–544.
 80. Chen, V.B., Arendall 3rd, W.B., Headd, J.J., Keedy, D.A., Immormino, R.M., Kapral, G.J., et al., (2010). MolProbity: all-atom structure validation for macromolecular crystallography. *Acta Crystallogr. D Biol. Crystallogr.* **66**, 12–21.